Antireflective all-dielectric metamaterials for thermophotovoltaic systems based on multiresonance

Yujie Yi [a], Zhiheng Xu [a,b,*], Ting Cai [a], Yong Chen [a], Zhi Yang [a], Yunpeng Liu [a,b], Xiaobin Tang [a,b,**]

[a] Department of Nuclear Science and Technology, Nanjing University of Aeronautics and Astronautics, Nanjing, 210016, China
[b] Key Laboratory of Nuclear Technology Application and Radiation Protection in Aerospace, Ministry of Industry and Information Technology, Nanjing, 211106, China

ARTICLE INFO

ABSTRACT

The efficient utilization of energy is essential for the normal and effective operation of photovoltaic (PV) cells in thermophotovoltaic (TPV) systems. In this work, a broadband metamaterial antireflective coating (ARC) is proposed to reduce the reflection losses, and Mie and Fabry–Pérot multiple resonances are used to optimize the performance of TPV systems. Simulations and analyses are carried out using finite-difference time-domain method and multipole decomposition to study the implementation of multiresonance responses of silicon resonator nanoarrays. The designed ARC exhibits an excellent average reflectivity of 1.71% in the near-infrared band, which significantly reduces the surface Fresnel reflection. The corresponding output power of the TPV systems is increased by 24.58% through InGaAsP/InGaAsP/InGaAs triple-junction PV cells. The metamaterial ARC design strategy can be broadly applicable, covering numerous material types and a long wavelength range, allowing for flexible application in various demanding scenarios.

1. Introduction

Thermophotovoltaic (TPV) technology, which uses photovoltaic (PV) cells to convert thermal radiation spectrum into electrical energy, provides an environment-friendly route to renewable energy[1–4]. Improving efficiency is a goal that is still continuously pursued in the current phase. The energy conversion process in TPV is divided into two core steps: the thermal to optical conversion and the optical to electrical conversion. In the pursuit of maximum efficiency, optimizing the front emitter has become a key strategy. By tailoring the thermal radiation spectrum to accurately match with the response spectrum of PV cells, radiation energy losses are effectively reduced. This area of research has achieved remarkable progress[5–7]. Nevertheless, optimizing the performance at the receiving end is also a proven strategy [8,9]. Among many challenges, the problem of optical loss is particularly prominent, which significantly limits the conversion efficiency of PV cells. Specifically, Fresnel reflection arising from high refractive index difference between semiconductors and air will lead to 30% optical loss, which seriously restricts the output efficiency of PV cells. Antireflective coatings (ARCs) provide an effective remedy that helps increase the local density of light states in the active absorber layer and improve the external quantum efficiency of PV cells. Conventional single or multi-layered thin-film ARCs must satisfy the interference constraint that the refractive index of each layer is the geometric mean of the refractive indices of the surrounding layers and is limited by the thickness of each layer and the substrate [10–12]. This increases the difficulty of finding new materials with the desired refractive index. In addition, at long wavelengths, the thickness of the layers increases substantially, leading to increased light scattering and absorption, which is contrary to the original design intent of ARCs.

The artificial subwavelength microstructure of metamaterial ARCs offers a new way of thinking in the search for ideal-performance ARCs, which can provide higher performance than the conventional ARC designs. Previous works have focused on the use of metallic plasmonic nanostructures[13–17]. Although antireflective effects can be achieved by relying on plasmon resonance, the practical application of plasmonic nanostructures is still hampered by a number of practical difficulties. For example, the metal itself has a large ohmic loss [18], which inhibits the local surface plasmon resonance of metal nanoparticles; the metal surface is susceptible to oxidation, and the formed oxide film can alter the

---

optical properties of metal nanostructures [19,20]. All-dielectric nanostructures are gradually coming into the limelight [21,22]. According to Mie theory, the maximum achievable scattering efficiency for subwavelength particles under a given multipolar excitation depends only on the resonance frequency and not on the type of the material [23]. This theory suggests that high-refractive-index dielectric nanoparticles [24] (e.g., Si, Ge, and GaP) can be used to achieve many of the plasmonic effects observed in the scattering of light by metallic nanoparticles.

The unique low-loss resonant behavior of dielectric nanoparticles can induce many subwavelength resonance effects [25,26], as well as the coexistence and interference of strong magnetic and electric resonances [27–29], which provide additional degrees of freedom for optical manipulation. Given that the resonance of high-refractive-index dielectric nanoparticles is determined by their characteristic dimensions and the optical properties of the material itself, the resonance can be modulated effectively and conveniently. Pala et al. [30] indicated that a trapezoidal nanoresonator metasurface design can efficiently couple to broadband Mie resonators and guided mode resonances across the entire solar spectral range, thus providing broadband absorption enhancement. Lee et al. [31] proposed multiresonance light-trapping ARCs for ultrathin c-Si solar cells based on an array of Mie resonators with a bimodal size distribution, which resulted in a 48% increase in short-circuit current density (J_{sc}) and a power conversion efficiency of up to 11.2% at one solar irradiation compared with planar Si cells. The aforementioned studies on ARCs have mainly focused on PV cells absorbing the solar spectrum. Relatively few studies exist on ARCs applied to thermal radiation spectra with peaks in the near-infrared band.

In this work, a multiresonant metamaterial ARC suitable for TPV systems is proposed, which realizes double-dipping and wide reflectance characteristics in the near-infrared band with an average reflectance of 1.71%. The output power of the TPV system increased to 1157.31 mW/cm^2 when combined with the InGaAsP/InGaAsP/InGaAs triple-junction PV cell, significantly enhancing the photon energy capture efficiency. The coupled interactions between Mie and Fabry–Pérot (FP) resonances in nanopatterned layers are studied intuitively using a theoretical model based on finite-difference time-domain (FDTD) method and multipole decomposition. This design strategy is universal, can be applied to all high-refractive-index materials and different wavelength ranges, and can be widely used in absorbers, image sensors, and photodetectors.

2. Modeling and simulations

As shown in Fig. 1, the proposed all-dielectric metamaterial ARC consists of a thin layer of MgF$_2$ and ZnS at the bottom and Si nano-resonators at the top. Si is one of the most suitable materials for the manufacture of all-dielectric optical components [32,33], with a high-refractive-index and a relatively low optical loss in the visible and near-infrared wavelength ranges. The superposition of MgF$_2$ and ZnS thin layers can form a structure with decreasing refractive index, which leads to enhanced coupling to the window layer of the PV cell (AlInP) and to a reduction of the optical loss in the transmission of the light to the active absorber layer of the semiconductor. The optimal structural parameters of the designed ARC are Si nanostructures with upper edge length $a = 90$ nm, lower edge length $b = 170$ nm, height $h = 300$ nm, distance between unit cells $d = 80$ nm, and thickness of the lower thin layers of MgF$_2$ and ZnS of 30 nm and 40 nm, respectively. The selected PV cells are InGaAsP/InGaAsP/InGaAs triple-junction cells with a long wavelength response (800–1800 nm) suitable for TPV systems. The simulation domain in the x–y plane is set as periodic boundary conditions, and perfectly matched layers are applied in the z-direction in the FDTD simulation domain [34]. The electromagnetic waves are incident perpendicular to the metamaterial ARC, and the electric and magnetic field components of the electromagnetic waves are simultaneously parallel to the ARC plane. Palik data [35] are used for the simulated material properties.
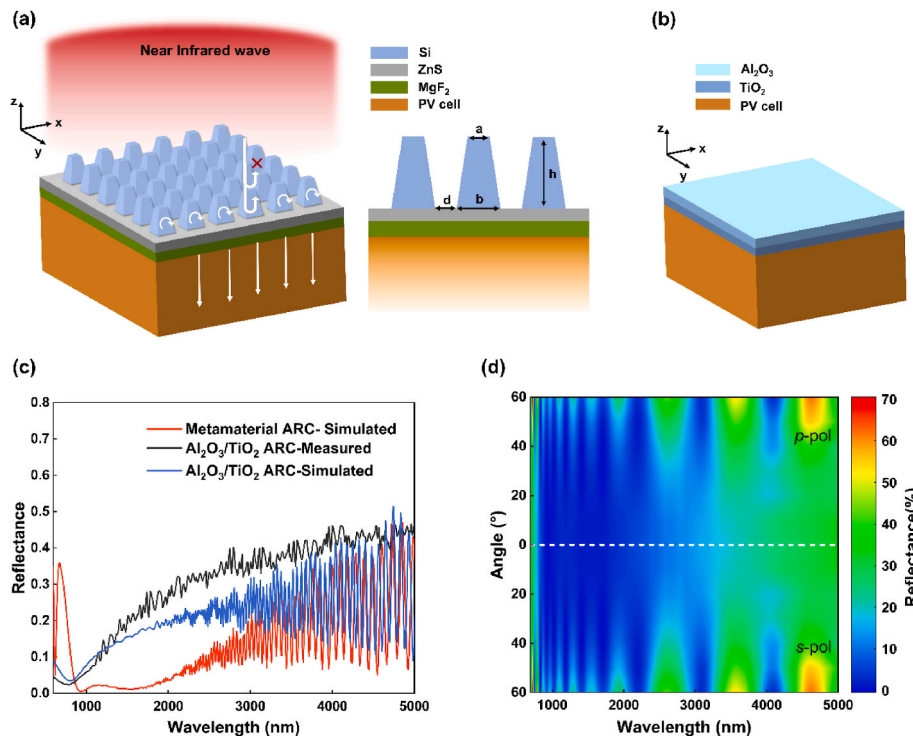

Fig. 1. Schematic structures of (a) the designed metamaterial ARC and (b) the conventional Al$_2$O$_3$/TiO$_2$ ARC. (c) Variation in reflectance with wavelength for Al$_2$O$_3$/TiO$_2$ and metamaterial ARC. (d) Variation in metamaterial ARC with angle of incidence and wavelength.

3. Results and analysis

3.1. Optical performance analysis

As shown in Fig. 1(c), the conventional Al_2O_3/TiO_2 antireflective ARC exhibits an average reflectivity of 12.55% in the same broadband range. By contrast, the designed metamaterial ARC exhibits excellent double-dip reflection performance in the spectral range of 850–1800 nm, with an average reflectivity of only 1.71%. The higher reflectivity in the 700–800 nm band helps minimize the effect of the conversion of high-energy photons into thermal energy on the performance of PV cells. The antireflection performance for non-normal angles of incidence is also satisfactory in practical applications. Fig. 1(d) shows the reflectance spectrum of (s, p) polarizations as a function of the angle of incidence (from 0° to 60°). p- and s-polarized lights have almost no effect on the reflectance spectrum. Multiple reflection peaks appear in the reflection spectrum with increasing angle of incidence. At the incident angle of 60°, the average reflectivity of the metamaterial ARC is 15.93%. No remarkable dependence of the reflectance spectral behavior on the angle of incidence in the range 0°–40° is observed. This wide-angle response and insensitivity to polarization demonstrate that well-designed arrays of fully dielectric nanostructures are beneficial for improving the overall performance of PV cells.

3.2. Physical mechanism analysis

Electromagnetic multipole expansion is used to analyze the electric and magnetic fields generated by spatially localized charges and currents and to study the interaction of electromagnetic fields with material systems [36,37]. Multipole decomposition based on induced current into the Cartesian electric dipole (ED, P), magnetic dipole (MD, M), toroidal dipole (TD, T), electric quadrupole (EQ, $Q_{\alpha\beta}$), and magnetic quadrupole (MQ, $M_{\alpha\beta}$) moments is performed using the following formulas in the long-wavelength approximation [38]:

$$P = \frac{1}{i\omega} \int J(r)d^3r \tag{1}$$

$$M = \frac{1}{2c} \int r \times J(r)d^3r \tag{2}$$

$$T = \frac{1}{10c} \int \{(r \cdot J(r))r - 2[r \cdot r]J(r)\}d^3r \tag{3}$$

$$Q_{\alpha\beta} = \frac{1}{2i\omega} \int \left\{ r_\alpha J_\beta(r) + r_\beta J_\alpha(r) - \frac{2}{3}[r \cdot J(r)]\delta_{\alpha\beta} \right\}d^3r \tag{4}$$

$$M_{\alpha\beta} = \frac{1}{3c} \int \{[r \times J(r)]_\alpha r_\beta + [r \times J(r)]_\beta r_\alpha\}d^3r \tag{5}$$

where ω is the frequency, c is the light velocity, and r is the position vector, denoted by r (x, y, z). The indices α and β indicate the Cartesian axes x, y, and z. The induced current density distributions $J(r)$ can be obtained from the electric field distributions $E(r)$ through the following equation:

$$J(r) = -i\omega\varepsilon_0(n^2 - 1)E(r) \tag{6}$$

where n is the refractive index of the structure, and ε_0 is the dielectric permittivity of free space. The corresponding total scattering cross section can be expressed as

$$I = \frac{2\omega^4}{3c^3}|P|^2 + \frac{2\omega^4}{3c^3}|M|^2 + \frac{2\omega^6}{3c^5}|T|^2 + \frac{\omega^6}{5c^5}\sum|Q_{\alpha\beta}|^2 + \frac{\omega^6}{20c^5}\sum|M_{\alpha\beta}|^2 \tag{7}$$

Fig. 2(a) illustrates the contributions of each radiating multipole moment to the far-field scattering power in Si nanostructures. Different multipole moments have different contributions to far-field scattering power, with the MD predominating in the short wavelength range of 600–900 nm. Specifically, at a wavelength around 650 nm, the TD, EQ, and MQ exhibit varying degrees of resonance peaks, whereas the ED and MD display troughs. At approximately 720 nm, the contribution from ED and MD resonance gives obvious peaks, especially MD, which produces a reflection peak in the reflection spectrum at 720 nm. It is noteworthy that at 935 nm, the scattering cross sections of ED and MD are equal, exhibiting spectrally overlapping electric and magnetic dipolar Mie-type resonances, and their phase difference approaches zero at this wavelength. This signifies that the TD and MD resonances interfere with and cancel each other out. This result exactly fulfils the first Kerker condition [21,39], which shows the suppressed backward scattering and intense forward scattering, mimicking the forward propagation behavior of the elementary Huygens' source [40–42] and achieving an almost zero reflection effect for the ARC, as shown by the first arrow in Fig. 2(b). At 1600 nm, the designed ARC exhibits a second dip, as indicated by the second arrow in Fig. 2(b). Comparing the reflection spectrum of the ARC with the Si nanostructures absent, it can be seen that the low reflection characteristic of the designed ARC at 1600 nm is attributed to the FP resonance induced by the Si nanostructures. In a word, the designed metamaterial ARC can support Mie and FP resonance incident light wave paths.

Fig. 3(a)–(d) show the magnetic (x–z plane) field distributions at 722, 935, 1600, and 3000 nm, respectively. The black dotted lines and the arrows in the field plots indicate the interface of the nanostructure and the field directions for magnetic fields, respectively. At wavelengths of 722 and 935 nm, almost the entire field amplitude is confined to the Si
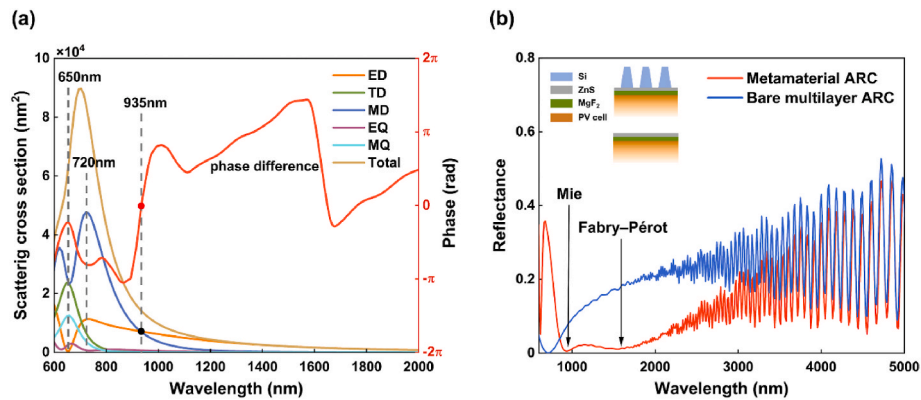

Fig. 2. (a) Scattering spectra of Cartesian ED, TD, MD, EQ, and MQ moments obtained by multipole decomposition; the red line indicates the phase difference of ED and MD moments. (b) Reflectance spectra of the designed ARC with (red line) and without (blue line) Si nanostructures. Measured reflectance minima are labeled with the corresponding antireflection mechanisms.
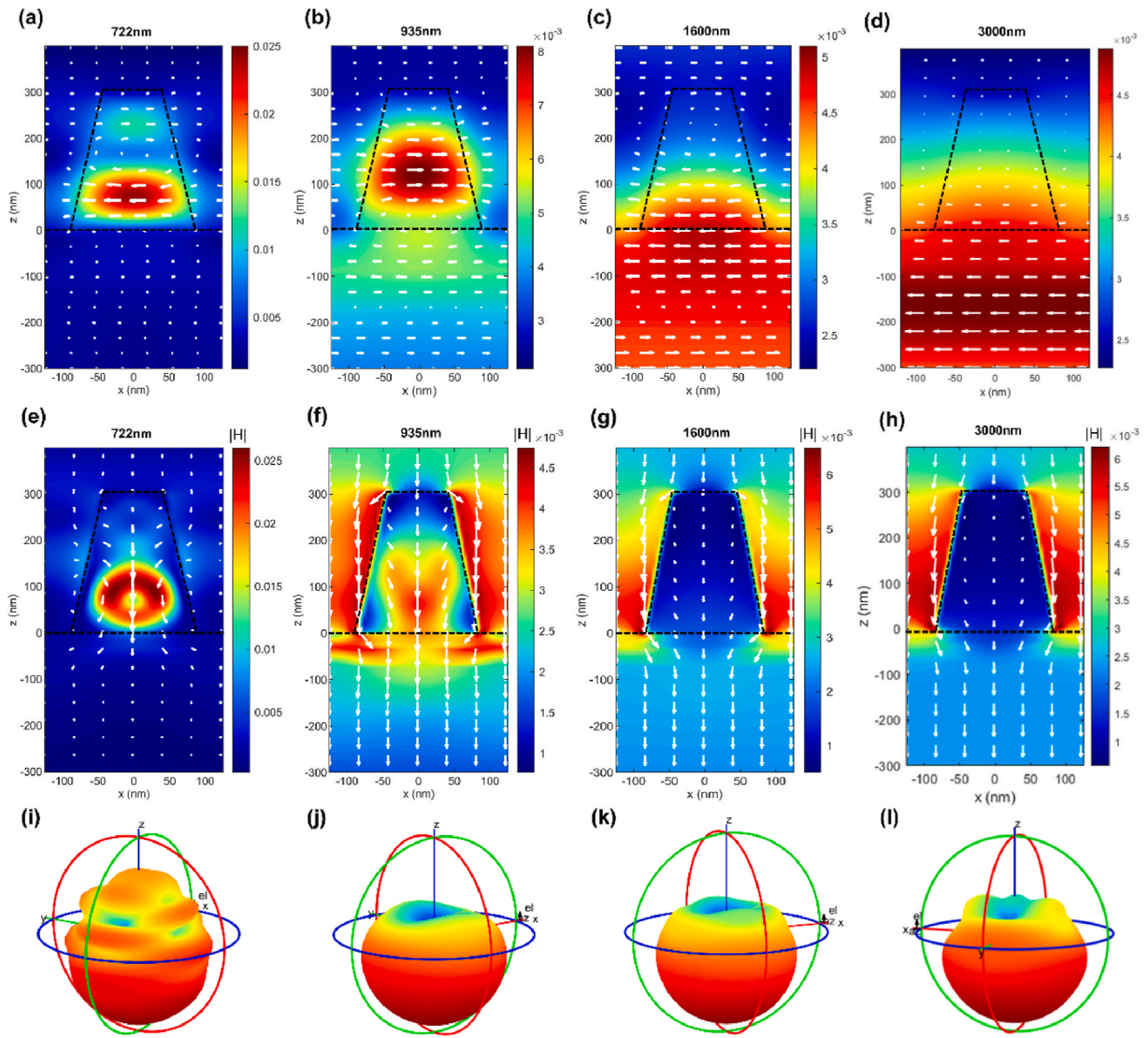
Fig. 3. Magnetic field |H| distribution (a)–(d), Poynting vector distribution (e)–(h), and far-field radiation (i)–(l) of the metamaterial ARC at 722, 935, 1600, and 3000 nm, respectively, in the x–z plane.

nanostructures and generates a transverse MD moment; by contrast, at 1600 and 3000 nm, this confinement disappears. As the increase of wavelength, the magnetic field intensity gradually decreases, which is consistent with the change of MD curve in Fig. 2(a). The distribution of Poynting vectors and the far-field radiation distribution at different wavelengths are used to investigate the optical transport of the designed

ARC, where the Poynting vectors represent the directed energy flux of the electromagnetic field. For the wavelength of 722 nm, almost all the energy is confined in the Si nanostructures, and the optical flow is not able to propagate downward, which leads to a large back reflection in the far field, as shown in Fig. 3(i). Fig. 3(f)–(h) show that the energy flow propagates vertically downward, and a light transport channel appears
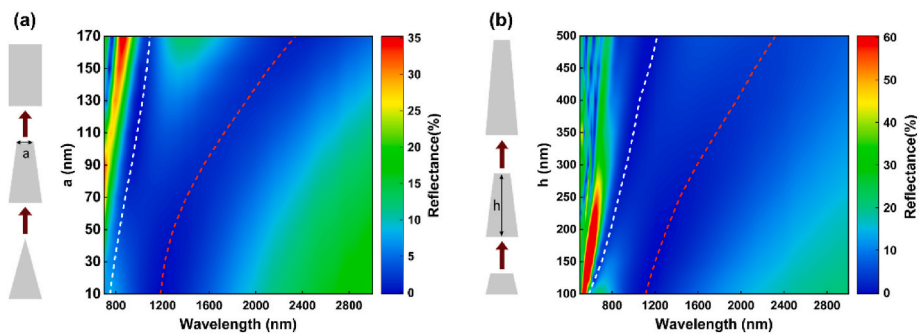

Fig. 4. Variations in the reflectivity of the designed ARC with top length *a* (a) and height *h* (b). The white dotted line shows the wavelength change when Si nanostructures with different sizes generate TD and MD resonances with the same intensity. The red dashed line indicates the minimum reflectance due to FP resonance.

at the bottom edge of the Si nanostructure. The energy of the region below the Si nanostructure increases visibly, and almost all the light is forward scattered in the corresponding far-field radiation pattern. This corresponds to the low reflection phenomenon at 935 nm and 1600 nm.

The reflectance of the designed ARC is further investigated as a function of the top length a and height h of the structure, as shown in Fig. 4(a) and (b). The white and red dashed lines represent the response mechanisms that produce double dip. As a and h increase, the resonance wavelengths of the excited Mie and FP resonances redshift, and the distance between them gradually increases, leading to an increasing distance between the corresponding reflection dips in the spectrum. This result is due to the increase in volume of the Si nanostructures, as well as the decrease in their sidewall slope. The size of nanostructures has a great influence on the shape of reflectance spectrum but a minimal effect on the magnitude of the reflectivity.

3.3. Performance improvement of photovoltaic cells

A high-performance ARC can make considerable light penetrate into PV cells and improve the photoelectric conversion efficiency. Fig. 5(b) shows the simulated EQE curves of solar cells with the designed ARC (solid line) and conventional Al_2O_3/TiO_2 ARC (dashed line). In comparison with the EQE of PV cells with conventional Al_2O_3/TiO_2 ARC, the EQE of PV cells with metamaterial ARC is significantly higher, indicating that more photocurrent is generated. A gradual increase in EQE is observed for each subcell from the top cell to the bottom cell, especially for the bottom cell with a maximum increase of 23%.

The enhancement in ARC absorption directly translates into an increase in J_{sc} and output power. The voltage and current density are defined by the following equation:

$$V = \frac{k_B T}{q} \sum_{i=1}^{3} \left[n_i \ln\left(\frac{J_{sc,i} - J}{J_{0,i}} + 1 \right) \right] \tag{8}$$

where k_B is the Boltzmann constant, T is the temperature, q is the elementary charge, $J_{0,i}$ is the reverse saturation current density of each subjunction cell, and $J_{sc,i}$ is the short-circuit current density of each subjunction cell, calculated from the blackbody thermal radiation power at certain temperature T.

$$J_{0,i} = q \int_{E_i}^{E_{i-1}} \frac{2\pi E^2}{h^3 c^3 \left[exp\left(\frac{E}{k_B T_a} \right) - 1 \right]} dE \tag{9}$$

$$J_{sc,i} = q \int_{E_i}^{E_{i-1}} \frac{q\lambda}{hc} EQE(\lambda) I(\lambda, T) d\lambda \tag{10}$$

where h is the Planck's constant, c is the light speed and $EQE(\lambda)$ is the external quantum efficiency of the PV cell. It represents the probability of absorption of a photon of wavelength λ by the PV cell and the production of an electron. The blackbody radiation power $I(\lambda, T)$ can be calculated as:

$$I(\lambda, T) = \frac{2\pi hc^2}{\lambda^5} \left[exp\left(\frac{hc}{k_B \lambda T} \right) - 1 \right] \tag{11}$$

For TPV system without considering the optimization of radiation spectrum by emitter, the formula for electrical power P and ideal TPV efficiency η_{TPV} is:

$$P = JV \tag{12}$$

$$\eta_{TPV} = \frac{P_{Max}}{\int_0^\infty \frac{2\pi hc^2}{\lambda^5} \left[exp\left(\frac{hc}{k_B \lambda T} \right) - 1 \right] d\lambda} \tag{13}$$

As shown in Fig. 5(c), the current density–voltage (J–V) characteristics of the TPV systems with different ARCs are calculated. The
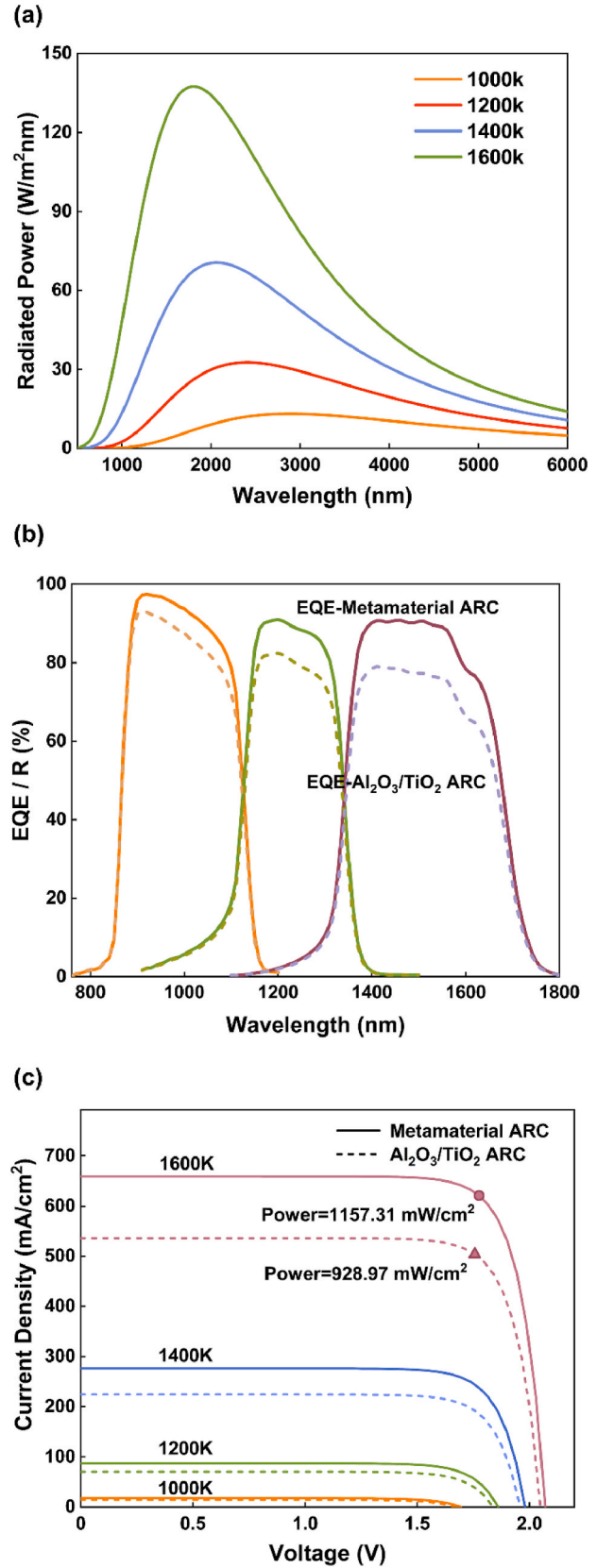
Fig. 5. (a) Radiant power spectra of the blackbody. (b) EQE/R of PV cells with metamaterial ARC and Al_2O_3/TiO_2 ARC. (c) J–V curves of PV cells with metamaterial ARC and Al_2O_3/TiO_2 ARC.

enhancement of the TPV systems with the designed metamaterial ARC is greater as the temperature increases, which is due to the redshift of the peak of the thermal radiated light with the increase in temperature. At 1600 K, compared with the J_{sc} based on the conventional Al_2O_3/TiO_2 ARC, the J_{sc} based on the metamaterial ARC increases to 692.12 mA/cm^2 from 562.45 mA/cm^2, which is a 23.05% increase, with a corresponding 24.58% increase in maximum output power (from 928.97 mW/cm^2 to 1157.31 mW/cm^2).

4. Conclusions

In summary, we demonstrate that an all-dielectric metamaterial ARC combining Mie and FP resonances for applications in TPV system, which achieves double-dip reflection in the NIR range. FDTD method and multipole decomposition are used to analyze the multiresonance response. Compared with that of the conventional Al_2O_3/TiO_2 ARC, the average reflectivity of the metamaterial ARC in the 850–1800 nm wavelength band decreases by 10.84%. Specifically, the overlapping of ED and MD modes and their phases results in almost zero reflection and maximum forward scattering at 935 nm through meeting the first Kerker condition. The output power of the TPV system increases by 24.58% when paired with InGaAsP/InGaAsP/InGaAs triple-junction PV cells, which significantly improves the efficiency of photon energy harvesting. This technology is expected to drive advances in optical components, transforming applications in fields such as photodetection, display technology, and energy conversion.

CRediT authorship contribution statement

Yujie Yi: Writing – original draft, Software, Methodology, Formal analysis, Data curation. **Zhiheng Xu:** Writing – review & editing, Supervision, Methodology, Funding acquisition, Formal analysis, Conceptualization. **Ting Cai:** Software, Formal analysis. **Yong Chen:** Writing – review & editing, Visualization. **Zhi Yang:** Writing – review & editing, Validation. **Yunpeng Liu:** Writing – review & editing, Funding acquisition. **Xiaobin Tang:** Writing – review & editing, Supervision, Methodology.

Declaration of competing interest

The authors declare that they have no known competing financial interests or personal relationships that could have appeared to influence the work reported in this paper.

Acknowledgments

Data availability

Data will be made available on request.

References

[1] K.F. Mustafa, S. Abdullah, M.Z. Abdullah, K. Sopian, A review of combustion-driven thermoelectric (TE) and thermophotovoltaic (TPV) power systems, Renew. Sust. Energ. Rev. 71 (2017) 572–584.

[2] B. Roy-Layinde, Demonstrating High Performing Thermophotovoltaic Systems Using Novel Cell-Side Architectures, University of Michigan, 2024. Ph.D. thesis.

[3] M.A. Prelas, C.L. Weaver, M.L. Watermann, E.D. Lukosi, R.J. Schott, D.A. Wisniewski, A review of nuclear batteries, Prog. Nucl. Energ. 75 (2014) 117–148.

[4] X. Wang, R. Liang, P. Fisher, W. Chan, J. Xu, Critical design features of thermal-based radioisotope generators: a review of the power solution for polar regions and space, Renew. Sust. Energ. Rev. 119 (2020) 109572.

[5] Z. Wang, D. Kortge, Z. He, J. Song, J. Zhu, C. Lee, H. Wang, P. Bermel, Selective emitter materials and designs for high-temperature thermophotovoltaic applications, Sol. Energ. Mat. Sol. C. 238 (2022) 111554.

[6] J. Tian, S. Shan, H. Wu, B. Zhang, G. Zhang, Z. Zhou, Performance of new designed meta-material absorbers/emitters reshaping solar spectrum to double-narrowband emissive spectrum for STPV power generation, Renew. Energ. 222 (2024) 119960.

[7] C. Meng, Y. Liu, Z. Xu, H. Wang, X. Tang, Selective emitter with core–shell nanosphere structure for thermophotovoltaic systems, Energy 239 (2022) 121884.

[8] B. Roy-Layinde, J. Lim, A. Lenert, S.R. Forrest, Integrated air-bridge tandem thermophotovoltaics with high efficiency over a broad heat source temperature range, ACS Energy Lett. 9 (2024) 2832–2839.

[9] L. Tang, H. Ye, J. Xu, A novel zinc diffusion process for the fabrication of high-performance GaSb thermophotovoltaic cells, Sol. Energ. Mat. Sol. C. 122 (2014) 94–98.

[10] J.Y. Huang, Y. Wang, G.T. Fei, S.H. Xu, Z. Zeng, B. Wang, TiO_2/ZnO double-layer broadband antireflective and down-shifting coatings for solar applications, Ceram. Int. 49 (2023) 11091–11100.

[11] H.K. Raut, V.A. Ganesh, A.S. Nair, S. Ramakrishna, Anti-reflective coatings: a critical, in-depth review, Energ. Environ. Sci. 4 (2011) 3779–3804.

[12] N. Sahouane, A. Necaibia, A. Ziane, R. Dabou, A. Bouraiou, M. Mostefaoui, A. Rouabhia, Realization and modeling of multilayer antireflection coatings for solar cells application, Mater. Res. Express 5 (2018) 065515.

[13] H.A. Atwater, A. Polman, Plasmonics for improved photovoltaic devices, Nat. Mater. 9 (2010) 205–213.

[14] K. Ueno, T. Oshikiri, Q. Sun, X. Shi, H. Misawa, Solid-state plasmonic solar cells, Chem. Rev. 118 (2017) 2955–2993.

[15] R.H. Fan, L.H. Zhu, R.W. Peng, X.R. Huang, D.X. Qi, X.P. Ren, Q. Hu, M. Wang, Broadband antireflection and light-trapping enhancement of plasmonic solar cells, Phys. Rev. B Condens. Matter Phys. 87 (2013) 195444.

[16] S.K. Sardana, V.S.N. Chava, E. Thouti, N. Chander, S. Kumar, S.R. Reddy, V.K. Komarala, Influence of surface plasmon resonances of silver nanoparticles on optical and electrical properties of textured silicon solar cell, Appl. Phys. Lett. 104 (2014) 073903.

[17] A. Ali, F. El-Mellouhi, A. Mitra, B. Aissa, Research progress of plasmonic nanostructure-enhanced photovoltaic solar cells, Nanomaterials 12 (2022) 788.

[18] P.B. Johnson, R.W. Christy, Optical constants of the noble metals, Phys. Rev. B 6 (1972) 4370.

[19] M. McMahon, R. Lopez, H.M. Meyer, L.C. Feldman, R.F. Haglund, Rapid tarnishing of silver nanoparticles in ambient laboratory air, Appl. Phys. B 80 (2005) 915–921.

[20] E. Zerbato, R. Farris, G. Fronzoni, K.M. Neyman, M. Stener, A. Bruix, Effects of oxygen adsorption on the optical properties of Ag nanoparticles, J. Phys. Chem. A 127 (2023) 10412–10424.

[21] A.I. Kuznetsov, A.E. Miroshnichenko, M.L. Brongersma, Y.S. Kivshar, B. Luk'yanchuk, Optically resonant dielectric nanostructures, Science 354 (2016) aag2472.

[22] S.A. Schulz, R.F. Oulton, M. Kenney, et al., Roadmap on photonic metasurfaces, Appl. Phys. Lett. 124 (2024) 260701.

[23] J.A. Schuller, M.L. Brongersma, General properties of dielectric optical antennas, Opt Express 17 (2009) 24084–24095.

[24] M.L. Brongersma, Y. Cui, S. Fan, Light management for photovoltaics using high-index nanostructures, Nat. Mater. 13 (2014) 451–460.

[25] K.X. Wang, Z. Yu, S. Sandhu, V. Liu, S. Fan, Condition for perfect antireflection by optical resonance at material interface, Optica 1 (2014) 388–395.

[26] E.F. Pecora, A. Cordaro, P.G. Kik, M.L. Brongersma, Broadband antireflection coatings employing multiresonant dielectric metasurfaces, ACS Photonics 5 (2018) 4456–4462.

[27] S. Jahani, Z. Jacob, All-dielectric metamaterials, Nat. Nanotechnol. 11 (2016) 23–36.

[28] P. Spinelli, M.A. Verschuuren, A. Polman, Broadband omnidirectional antireflection coating based on subwavelength surface Mie resonators, Nat. Commun. 3 (2012) 692.

[29] K. Koshelev, Y. Kivshar, Dielectric resonant metaphotonics, ACS Photonics 8 (2020) 102–112.

[30] R.A. Pala, S. Butun, K. Aydin, H.A. Atwater, Omnidirectional and broadband absorption enhancement from trapezoidal Mie resonators in semiconductor metasurfaces, Sci. Rep. 6 (2016) 31451.

[31] N. Lee, M. Xue, J. Hong, J. van de Groep, M.L. Brongersma, multi-resonant Mie resonator arrays for broadband light trapping in ultrathin c-Si solar cells, Adv. Mater. 35 (2023) 2210941.

[32] A.F. Cihan, A.G. Curto, S. Raza, P.G. Kik, M.L.J.N.P. Brongersma, Silicon Mie resonators for highly directional light emission from monolayer MoS_2, Nat. Photonics 12 (2018) 284–290.

[33] Y. Kivshar, A. Miroshnichenko, Meta-optics with Mie resonances, Opt Photon. News 28 (2017) 24–31.

[34] R. Alaee, C. Rockstuhl, I. Fernandez-Corbaton, An electromagnetic multipole expansion beyond the long-wavelength approximation, Opt Commun. 407 (2018) 17–21.

[35] Palik, D.J.A.P. Edward, Handbook of Optical Constants of Solids, Academic press, 1985.

[36] R. Alaee, C. Rockstuhl, I. Fernandez-Corbaton, Exact multipolar decompositions with applications in nanophotonics, Adv. Opt. Mater. 7 (2019) 1800783.

[37] P. Grahn, A. Shevchenko, M. Kaivola, Electromagnetic multipole theory for optical nanomaterials, New J. Phys. 14 (2012) 093033.

[38] H. Hasebe, H. Sugimoto, T. Hinamoto, M. Fujii, Coupled toroidal dipole modes in silicon nanodisk metasurface: polarization independent narrow band absorption and directional emission, Adv. Opt. Mater. 8 (2020) 2001148.

[39] W. Liu, Y.S. Kivshar, Generalized Kerker effects in nanophotonics and meta-optics, Opt Express 26 (2018) 13085–13105.

[40] A.E. Krasnok, A.E. Miroshnichenko, P.A. Belov, Y.S. Kivshar, Huygens optical elements and Yagi—uda nanoantennas based on dielectric nanoparticles, JETP Lett. 94 (2011) 593–598.

[41] J.M. Geffrin, B. García-Cámara, R. Gómez-Medina, P. Albella, L. Froufe-Pérez, C. Eyraud, A. Litman, R. Vaillon, F. González, M. Nieto-Vesperinas, Magnetic and electric coherence in forward-and back-scattered electromagnetic waves by a single dielectric subwavelength sphere, Nat. Commun. 3 (2012) 1171.

[42] Y. Kivshar, All-dielectric meta-optics and non-linear nanophotonics, Natl. Sci. Rev. 5 (2018) 144–158.